

Zeeman Effekt

FORTGESCHRITTENEN PRAKTIKUM I

Gruppe PBB3

Corvin Lenz (7034864)
Fabian Voltz (7038209)

05.November 2024

Betreuer:

Saran Shaju
AG Eschner



**UNIVERSITÄT
DES
SAARLANDES**

Contents

Introduction	2
1 Theoretical principles	2
1.1 Quantum-mechanical description	2
1.1.1 Strength of dipole transitions and Clebsch-Gordan coefficients	3
1.1.2 Angular dependence of dipole radiation	4
1.1.3 Classification of the Zeeman effect	5
1.2 Functionality of optical elements	5
1.2.1 The Lyot filter (LF)	6
1.2.2 The Fabry-Pérot interferometer (FPI)	6
2 Measurement and experimental setup	7
2.1 Preparation	8
3 Measurements with evaluation	9
3.1 Correction for the piezo crystal	9
3.2 Spectrum of the D_1 - and D_2 -line	10
3.3 Landé-factors	12
3.4 Clebsch-Gordan coefficients	13
4 Conclusion and discussion of the results	14
Referenzen	15

Introduction

The so-called Zeeman-effect describes the splitting of atomic spectral lines under the presence of an external magnetic field. It was discovered by Pieter Zeeman in 1896 [1] and Hendrik Antoon Lorentz was given a Nobel prize in 1902 for a physical explanation [2]. In general the splitting is due to an angular momentum like the orbital angular momentum or intrinsic angular momentum of the particle. Further classification follows in a later part.

The discovery of this effect was an early contact with quantum-mechanics and it had a big influence on today's knowledge. It was as important for practical applications like for the zeeman-slower, which is a very important part in investigating single atoms [3].

In this experiment, the Zeeman splitting of two spectral lines of a sodium vapor lamp is examined more closely in order to draw conclusions about the atomic transitions. In addition, the handling of optical setups is trained and theoretical knowledge is confirmed.

1 Theoretical principles

1.1 Quantum-mechanical description

To fully understand the Zeeman effect, here is a brief theoretical explanation.

As fermions, electrons in the atom not only have an orbital angular momentum \mathbf{L} but also an intrinsic angular momentum \mathbf{S} , also called *Spin*. The total angular momentum results in $\mathbf{J} = \mathbf{L} + \mathbf{S}$. If we now take a closer look at the electron, it immediately becomes clear that it has a magnetic moment:

$$\boldsymbol{\mu}_J = -g_J \frac{\mu_B}{\hbar} \mathbf{J}$$

Here μ_B denotes the Bohr magneton and g_J the Landé g-factor, each defined as

$$\mu_B = \frac{e\hbar}{2m_e} \quad \text{und} \quad g_J = \frac{g_S + g_L}{2} - \frac{g_S - g_L}{2} \frac{L(L+1) - S(S+1)}{J(J+1)} \quad (1)$$

with the Landé g-factor of the orbital angular momentum $g_L = 1$ and the spin $g_S \approx 2$ of the electron.

The Schrödinger equation, which completely describes a quantum mechanical system, can be solved exactly for an electron in a hydrogen atom. The Hamiltonian operator of such an electron is

$$\hat{H}_0 = \frac{\mathbf{p}^2}{2m} - \frac{e^2}{r} \quad (2)$$

The solutions are known, which is why they are not discussed in detail here. What is important at this point is the corresponding energy [4]

$$E_{nl} = -\frac{R}{n^2} \quad n \in \mathbb{N} \quad (3)$$

If the electron is now in a magnetic field \mathbf{B} in whose direction we place the z -axis, the Hamilton is supplemented by the following so-called *Zeeman term*

$$\hat{H}_{Ze} = -\boldsymbol{\mu}_J \cdot \mathbf{B} = g_J \frac{\mu_B}{\hbar} (\mathbf{J} \cdot \mathbf{B}) \quad (4)$$

Under the premise that the z -axis and \mathbf{B} -field are parallel to each other, the energy shift due to the Zeeman-Hamilton results in

$$E_{Ze} = m_j g_J \mu_B B \quad (5)$$

At this point, the quantum numbers that completely describe an electron are discussed.

n	Principal quantum number	$n \in \mathbb{N}$
l	Azimuthal quantum number	$0 \leq l < n \wedge l \in \mathbb{N}$
m_j	magnetic quantum number	$-l \leq m_j \leq l \wedge m_j \in \mathbb{N}$
m_s	Spin quantum number	$\pm \frac{1}{2}$

We see from Equation 3 and Equation 5 that the fundamental energy is m_j -fold degenerated, but this degeneracy is canceled by the applied magnetic field. By splitting those energy levels, new inter-atomic transitions become possible, resulting in the splitting of the spectral lines.

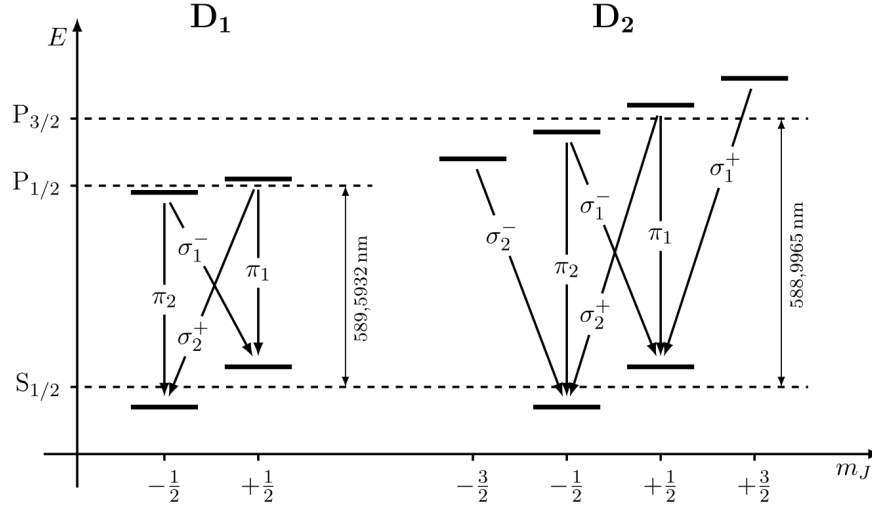


Figure 1.1: Energy term diagram of the two D-lines, figure from [5]

The dominant spectral lines of the sodium lamp used are the D -lines. The nomenclature follows from the Fraunhofer lines. The energetic splitting in the presence of a magnetic field is shown schematically in Figure 1.1. The energy levels involved are the $S_{1/2}$ and $P_{1/2}$ levels for the D_1 line and the $S_{1/2}$ and $P_{3/2}$ levels for the D_2 line.

The two levels with $J = 1/2$ are each split twice, the third level four times. If we consider optical transitions in the dipole approximation, the selection rule is $\Delta m_J = 0, \pm 1$, so that four transitions are possible for the first D line and six for the second. These are named according to their polarization, the transitions with $\Delta m_J = \pm 1$ emit circularly polarized photons and are referred to as σ^\pm . Transitions with $\Delta m_J = 0$ result in linearly polarized photons parallel to the z -axis, so those are called π [5].

1.1.1 Strength of dipole transitions and Clebsch-Gordan coefficients

The dipole transition can be seen as a coupling of two atomic states with different angular momenta with a photon. Therefore we need a short introduction to the formalism:

We want to take a look at the two states $|k_1, j_1, m_1\rangle$ and $|k_2, j_2, m_2\rangle$ with corresponding eigenvectors in their eigenbasis

$$\begin{aligned} \mathbf{J}_1^2 |k_i, j_i, m_i\rangle &= j_i(j_i + 1)\hbar^2 |k_i, j_i, m_i\rangle \\ J_{iz} |k_i, j_i, m_i\rangle &= m_i\hbar |k_i, j_i, m_i\rangle \end{aligned}$$

The basis of the coupled system can be written as a tensor product of the individual ones

$$|k_1, k_2; j_1, j_2; m_1, m_2\rangle = |k_1, j_1, m_1\rangle \otimes |k_2, j_2, m_2\rangle \quad (6)$$

so that the resulting angular momentum can be seen as $\mathbf{J} = \mathbf{J}_1 + \mathbf{J}_2$ but one can see that the coupled states are not eigenstates of \mathbf{J}^2 . Therefore we introduce $|J, M\rangle$ as the eigenvectors of \mathbf{J}^2 and J_z with the corresponding eigenvalues J and M .

Now we want to write $|J, M\rangle$ as a linear combination of the uncoupled states, which is possible due to the states in Equation 6 forming a orthonormal basis. This results in

$$|J, M\rangle = \sum_{m_1=-j_1}^{j_1} \sum_{m_2=-j_2}^{j_2} |k_1, k_2; j_1, j_2; m_1, m_2\rangle \langle k_1, k_2; j_1, j_2; m_1, m_2 | J, M\rangle \quad (7)$$

The coefficients $\langle k_1, k_2; j_1, j_2; m_1, m_2 | J, M\rangle$ in Equation 7 are called the *Clebsch-Gordan-Coefficients* (short: CGK).

When we look at the decay from the $P_{1/2}$ -State $|J, M_j\rangle = |\frac{1}{2}, \frac{1}{2}\rangle$ in the D_1 -Line we need to express it in terms of the ground states

$$\begin{aligned} \left| \frac{1}{2}, \frac{1}{2} \right\rangle &= c_1 \left| 1, \frac{1}{2}; 1, -\frac{1}{2} \right\rangle + c_2 \left| 1, \frac{1}{2}; 1, +\frac{1}{2} \right\rangle \\ &+ c_3 \left| 1, \frac{1}{2}; 0, -\frac{1}{2} \right\rangle + c_4 \left| 1, \frac{1}{2}; 0, +\frac{1}{2} \right\rangle \\ &+ c_5 \left| 1, \frac{1}{2}; -1, -\frac{1}{2} \right\rangle + c_6 \left| 1, \frac{1}{2}; -1, +\frac{1}{2} \right\rangle \end{aligned}$$

where c_{1-6} are the CGK which can be extracted from several tabular. Here only c_1 and c_4 are non-zero [5]:

$$\left| \frac{1}{2}, \frac{1}{2} \right\rangle = \sqrt{\frac{2}{3}} \left| 1, \frac{1}{2}; 1, -\frac{1}{2} \right\rangle - \sqrt{\frac{1}{3}} \left| 1, \frac{1}{2}; 0, \frac{1}{2} \right\rangle$$

For later analysis we need the CGK for the D_1 - and D_2 -lines for transitioning to the $S_{1/2}$ -state:

m_j	$-1/2$	$1/2$
$-1/2$	$\sqrt{1/3}$	$\sqrt{2/3}$
$1/2$	$-\sqrt{2/3}$	$-\sqrt{1/3}$

Table 1: CGK for D_1 -Line

m_j	$-3/2$	$-1/2$	$1/2$	$3/2$
$-1/2$	1	$\sqrt{2/3}$	$\sqrt{1/3}$	none
$1/2$	none	$\sqrt{1/3}$	$\sqrt{2/3}$	1

Table 2: CGK for D_2 -Line

The columns in Table 1 and Table 2 describe the m_j of $P_{1/2}$ or $P_{3/2}$ and the rows the m_j for $S_{1/2}$.

1.1.2 Angular dependence of dipole radiation

We saw in subsection 1.1 that the emitted photons from varying transitions can have different polarizations like circular for σ - and linear for π -transitions. Therefore, the different polarizations result in radiated intensity in different directions.

To further understand this, we will call $\mathbf{r}_{ba} = \langle j_b m_b | \mathbf{r} | j_a m_a \rangle$ the amplitude of the transition from $|j_b m_b\rangle$ to $|j_a m_a\rangle$. This amplitude can be interpreted as an oscillation and thus the electric field takes the form

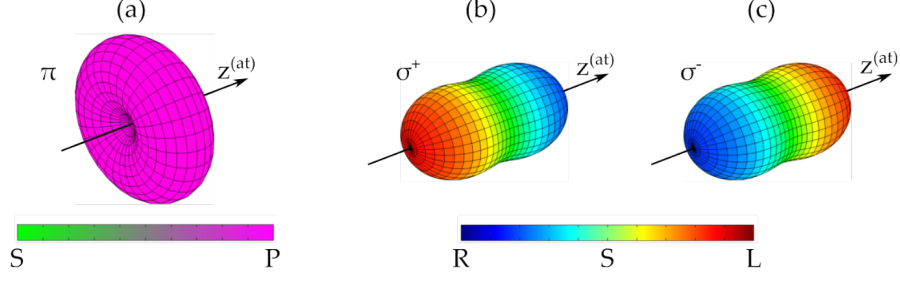


Figure 1.2: Intensity profile of dipole radiation for π -transition (a) and σ^\pm -transition (b) and (c). R and L describe right- and leftcircular polarization and S and P linear polarizations. Figure from [5]

$$\begin{aligned} \mathbf{E}(\mathbf{r}) \propto \exp(i\omega_b t) \mathbf{r}_{ba} \exp(-i\omega_a t) &= \langle m_b | r_{-1} | m_a \rangle (\mathbf{e}_{-1} \exp(-i\omega_{ba} t))^* \\ &+ \langle m_b | r_0 | m_a \rangle (\mathbf{e}_0 \exp(-i\omega_{ba} t))^* \\ &+ \langle m_b | r_{+1} | m_a \rangle (\mathbf{e}_{+1} \exp(-i\omega_{ba} t))^* \end{aligned}$$

Here \mathbf{e}_i are the basis vectors in the spherical basis so that $\mathbf{e}_{\pm 1}$ describes a circular oscillation in σ^\pm direction and \mathbf{e}_0 a π -linear one [5].

The radiated intensity of each case is shown in Figure 1.2 by defining θ_k as the angle between the direction of propagation $z^{(ph)}$ of the photon and the axis of the quantization $z^{(at)}$. For the linear oscillation this yields the form

$$I(\theta_k) \propto \langle m_b | r_0 | m_a \rangle^2 \sin^2(\theta_k) \propto \sin^2(\theta_k)$$

and for the circular one it is

$$I(\theta_k) \propto \frac{\langle m_b | r_{\pm 1} | m_a \rangle^2}{2} (1 + \cos^2(\theta_k)) \propto \frac{1 + \cos^2(\theta_k)}{2}$$

1.1.3 Classification of the Zeeman effect

One can differentiate between two different effects: The normal Zeeman effect and the anomalous Zeeman effect

First discovered was the normal Zeeman effect [1]. We saw earlier in subsection 1.1 that the splitting is due to the angular momenta \mathbf{L} and \mathbf{S} . When the spin of an atom is zero, e.g. for even number of electrons only the orbital angular momentum contributes to the splitting. This results in an odd number of different spectral lines due to L having integer eigenvalues.

The anomalous Zeeman effect describes the case where \mathbf{L} and \mathbf{S} are non-zero. Thus we can interpret the normal Zeeman effect as a special case of the anomalous one. The nomenclature comes from the spin not being discovered when the effect was first seen. It differs in an even number of spectral lines in comparison to the normal one. Due to sodium having an odd number of electrons and thus a non-zero net spin we will see the anomalous Zeeman effect in this experiment.

1.2 Functionality of optical elements

Now that the theoretical side of the Zeeman-effect is covered, we need to take a look at the individual elements, which are build in to our setup, so that we can observe the splitting of spectral lines and differ between D_1 - and D_2 -frequencies. Although several elements were necessary for the experimental construction, we will focus

in the following on the *Lyot filter* and the *Fabry-Pérot interferometer*, as these are the most important tools for our purpose.

1.2.1 The Lyot filter (LF)

One of the optical elements used in the setup is the so called *Lyot filter*, which has a influence on the polarization of two rays with different wavelengths λ . This filter is constructed by two polarizer and a birefringent crystal as depicted in Figure 1.3.

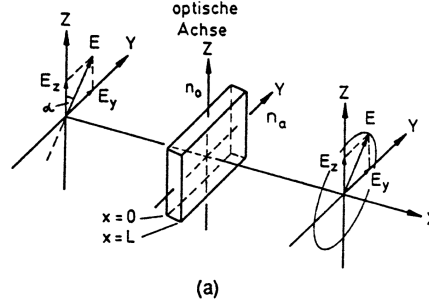


Figure 1.3: construction of a Lyot filter, figure from [6]

To get a brief glimpse of the function and components of the *Lyot filter*, we will discuss this optical element with respect to our experimental setup. The light of the sodium lamp emits the characteristic D_1 and D_2 lines, which will pass the first polarization filter, so that they overlap and have the same linear polarization. Now the collinear oscillating waves will propagate through the crystal with anisotropic refractive index. This leads to the same polarization of both lines but they will now oscillate orthogonal to each other. Therefore it is easy to pick out one specific line for measurement using the second and last polarization filter.

1.2.2 The Fabry-Pérot interferometer (FPI)

Another important element is the *Fabry-Pérot interferometer*, which will be mounted behind the previous explained *Lyot filter*. The element's function is based on the optical path difference of parallel aligned waves, reflecting off of walls in the cavity with length d . This cavity consists of two highly reflective mirrors, which are facing each other, so that when light transmits through the non-reflecting external side of one mirror, it can either transmit through the second one or it will continue oscillate in the cavity.

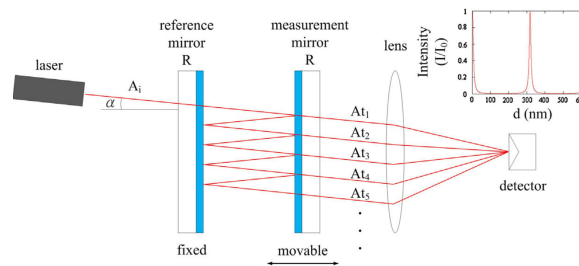


Figure 1.4: ray path in a FPI, figure from [7]

After several oscillations it will eventually leave the system but with a certain path difference with respect to light, which has left earlier/later. To visualize the optical path difference and therefore the effect of an FPI, one can use a converging lens to observe interference on a screen. One remarkable property of the FPI is the so called *Free-Spectral-Range* or short *FSR*. When observing the transmission pattern in dependence of the frequency, one can see a periodic behavior, so that certain frequencies will be equally transmitted with a relative distance of $\delta\nu$, the FSR.[8]

$$\delta\nu = \nu_{m+1} - \nu_m = \frac{c}{2d} \quad (8)$$

For fine adjusting of the cavity spacing a piezo crystal is used, which will change length as a response to applied voltage. Different resonator lengths will change the appearance of interference, i.e. the spacing between different orders.

2 Measurement and experimental setup

Before we can measure anything, we have to build our setup for the experiment depicted in [Figure 2.1](#).

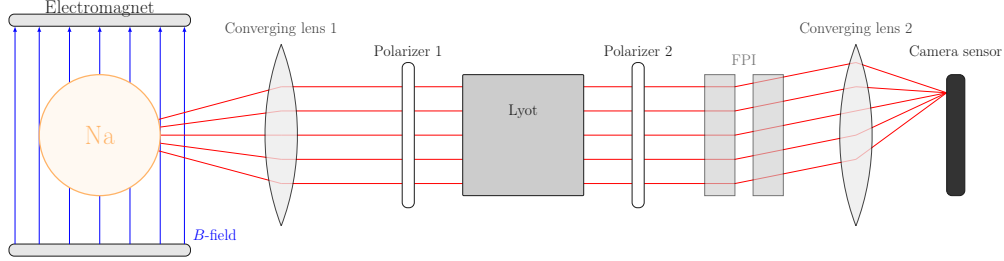


Figure 2.1: Setup

To begin with, a sodium lamp will be placed into an electromagnet, so that the magnetic field acting on the emitted light can be adjusted by changing the current in the magnet. To minimize the radiation loss by divergent rays, a converging lens is placed in front of the magnet so that the sodium lamp is located at the focal point of the lens. By doing this, the emitted light gets bundled and incoming rays parallelized. For an optimal usage of the Lyot filter, the parallelized light needs to be linear polarized.

We discussed in [subsection 1.1](#) that the σ^\pm -transitions are circular polarized, when looking parallel to the magnetic field. By changing our perspective to looking perpendicular to the magnetic field, both the π - and σ -transitions appear to be linear polarized, each perpendicular to each other. This is shown in [Figure 2.2](#). Due to the fact that the magnetic field in our setup is parallel to the table we see that the π -transitions are also parallel polarized to the table and the σ -transitions orthogonal to the tabletop. This will be important later to filter out each component with the first polarizer.

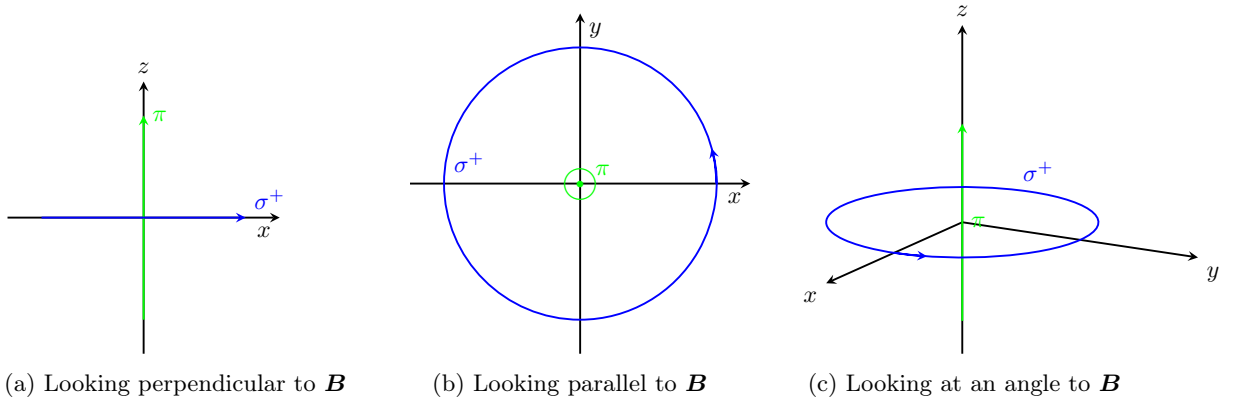


Figure 2.2: Illustration on how the perspective changes the observed polarization for $\mathbf{B} \propto \hat{z}$

After filtering the π - and σ -transitions, one can place a second polarizer right behind the Lyot filter, to choose one of the two D-lines, which then will be examined. In order to know which of those lines one has chosen, we need to add a Fabry-Pérot interferometer to make a statement about the observed spectrum. The parallel rays from the FPI, which have an optical path difference, will now be bundled by a second converging lens and measured by a camera sensor placed at the focal point of the lens.

2.1 Preparation

To begin with, we needed to verify the homogeneity of the magnetic field. That's why we were given an hall-probe to measure the magnetic field in different positions for a constant current. We choose $I = 5 \text{ A}$ and this data can be seen in Figure 2.3. The magnetic field was pretty homogeneous and differs only by a few mT , which is sufficient for our needs.

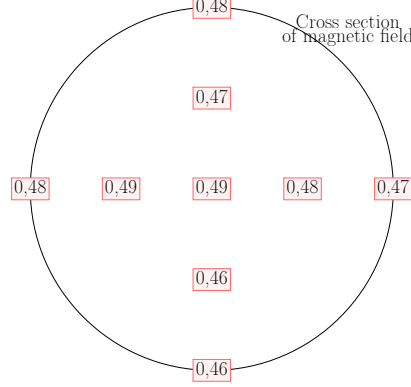


Figure 2.3: Magnetic induction in various positions of the \mathbf{B} -field to verify the homogeneity, values in mT for $I = 5 \text{ A}$

Additionally we need some sort of function to get the magnetic induction because later we can't measure it directly with the hall-probe but just got the current from the power supply which drives the electro magnet. Therefore we measured the magnetic induction for many various currents to fit a linear slope between these points which is possible because $B \propto I$. This result is shown in Figure 2.4.

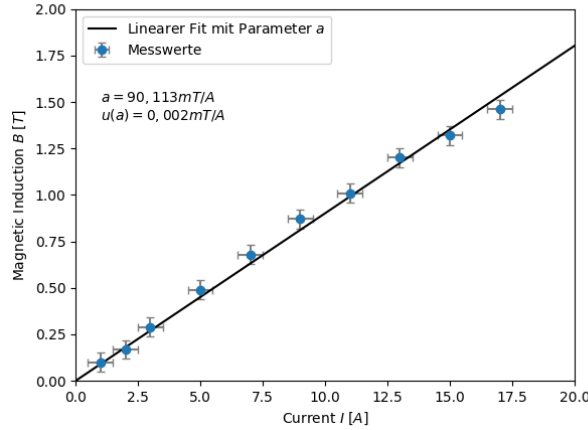


Figure 2.4: Magnetic induction from measured data

Now we got the function

$$B(I) = 90,113 \cdot 10^{-3} \frac{T}{A} \cdot I \quad (9)$$

to translate between B and I .

For further investigations, we need the length of the FPI chosen exactly so that both D-Lines overlap on the camera, given that the Lyot-filter is set up accordingly. This was already the case but to verify this we needed to know at what positions of the last polarizer which line can be seen. This was realized by looking at the number of spectral lines on the live screen from the camera. Continuously turning the polarizer revealed first the four lines from the D_1 -lines at $\varphi_1 = 78^\circ$. Further turning made investigating the six spectral lines of the

D_2 -line at $\varphi_2 = 168^\circ$ possible, exactly 90° apart from the position for the D_1 -line. With this in mind we set the polarizer to $\varphi = 123^\circ$ so that the full spectrum of the D -line can be seen and they indeed overlapped. To later calculate the FSR $\delta\nu$ we need to know the exact distance between the mirrors of the FPI. From measuring the position x of the installed micrometer screw gauge we can calculate the distance L :

$$L = x - 5,94\text{mm} + 1,4\text{mm} = 6,72\text{mm} - 5,94\text{mm} + 1,4\text{mm} = 2,18\text{mm}$$

This can be retraced by the schematic in [Figure 2.5](#).

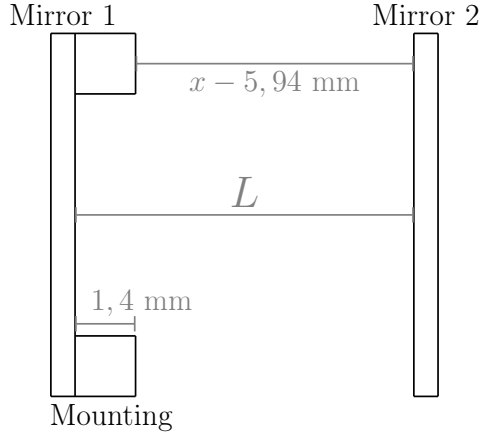


Figure 2.5: Schematic for the dimensions inside the FPI, not to scale

After further adjusting the alignment of the FPI so that we got symmetric and sharp rings on the camera we could continue with the measurements.

3 Measurements with evaluation

3.1 Correction for the piezo crystal

The program we used to control the piezo crystal which moves the FPI uses it's own units, called *Integervales*. It ranges approximately from 0 to 16000. Due to the fact that we need the frequency difference between the peaks for corresponding integervales we must find a function to translate between those integervales and relative frequency's.

However the crystal does not move linearly so we need a quadratic correction function. For that we need to calculate the free spectral range first:

$$\delta\nu = \frac{c}{2L} \approx 68,7597\text{GHz} \quad (10)$$

Now we know that two rings from the FPI for the same wavelength are roughly 70 GHz apart. We measured the intensity in one ring on the camera sensor over the full spectrum of the piezo. This gave us three sharp peaks to work with, as seen in [Figure 3.1a](#).

Assuming the position ν_{rel} of the piezo in terms of relative frequency would follow the form $\nu_{rel}(x) = ax^2 + bx$ with x being the integervalue and the fact that we know the position of the three peaks from our fit in [Figure 3.1a](#) we can now calculate the parameters a and b :

$$\nu_{rel}(\mu_2) - \nu_{rel}(\mu_1) = a(\mu_2^2 - \mu_1^2) + b(\mu_2 - \mu_1) = \delta\nu \quad (11)$$

$$\nu_{rel}(\mu_3) - \nu_{rel}(\mu_2) = a(\mu_3^2 - \mu_2^2) + b(\mu_3 - \mu_2) = \delta\nu \quad (12)$$

This uses the fact that all peaks are spaced exactly with the FSR. By combining Equation 11 and Equation 12 and the values from Figure 3.1a we can determine the parameters as

$$a = 88.7196 \text{ Hz}^{-1}$$

$$b = 11901628.2460 \text{ Hz}^{-1}$$

And thus the correction function is shown in Figure 3.1b and takes the form:

$$\nu_{rel}(x) = 88,7 \text{ Hz}^{-1} \cdot x^2 + 11,9 \text{ GHz}^{-1} \cdot x \quad (13)$$

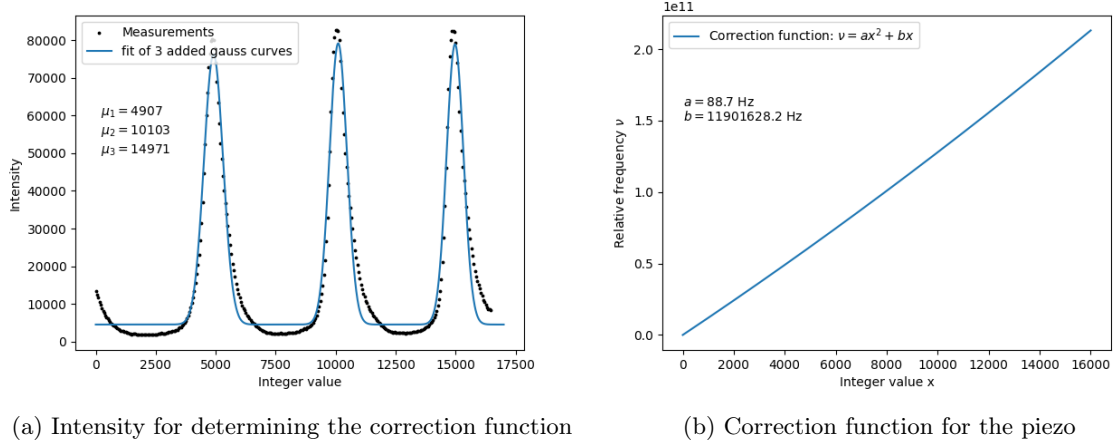


Figure 3.1: Plots necessary for determining the correction function

3.2 Spectrum of the D_1 - and D_2 -line

After handling the conversion between integervales and relative frequencies we can continue with the real analysis.

Like mentioned before, for collecting our data we set two rings centered around the origin of the FPI-rings in the software. When we start a measurement, the software sends voltages to the piezo so that it moves and the program sums over all data between the two previously mentioned rings. We then get a spectrum with intensities for each integervalue, which we can convert to a relative frequency according to Equation 13.

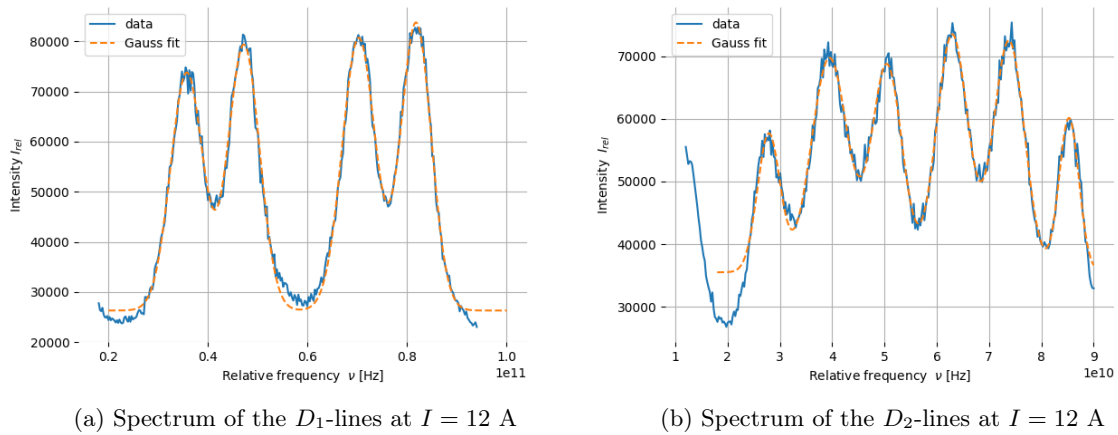


Figure 3.2: Measured spectrum of the D_1 - and D_2 -line in the magnetic field with a correspondign fit

We collected data for each of the D -lines for various currents $I \in \{9A, 10A, 11A, 12A\}$ and respecting magnetic field. For our analysis we chose the current for that the spectrum appears the clearest. Criteria to chose the *best* current were the sharpness of the peaks and their amplitude. Those criteria led to us using $I = 12A$ for both lines. The corresponding spectra are shown in [Figure 3.2](#).

For further investigation we need some specific data from each spectrum. Therefore we fitted the expected function, which was the sum of three gauss curves for the D_1 -line and the sum of six gauss curves for the second one. Because each gauss curve is uniquely defined by three parameters μ_i, σ_i and A_i , each fit needs at least 12 or 18 parameters. Additionally another parameter must be introduced to shift the whole spectrum up and down because of our base level not being zero due to noise. This leaves us with 13 parameters for the D_1 -fit and 19 for the D_2 -fit.

For our python code to find the optimal fit parameters it needs relatively precise estimations for those. This was made possible by guessing the three parameter for each gauss curve and the noise level. This leaves us with the fit shown in [Figure 3.2](#).

Our parameters are given in [Table 3](#) and [Table 4](#).

Peak	1	2	3	4
$\mu_{1,i}$ in GHz	35,73	47,21	70,27	81,80
$A_{1,i} \cdot 10^{-4}$	4,74	5,30	5,44	5,74
Transition	σ_1^-	π_1	π_2	σ_2^+

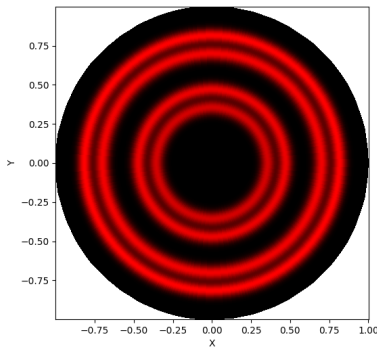
Table 3: Fit parameters for D_1 -Line

Peak	1	2	3	4	5	6
$\mu_{2,i}$ in GHz	27,87	39,49	50,48	62,96	73,81	85,30
$A_{2,i} \cdot 10^{-4}$	2,206	3,420	3,302	3,795	3,696	2,462
Transition	σ_1^-	σ_2^-	π_1	π_2	σ_1^+	σ_2^+

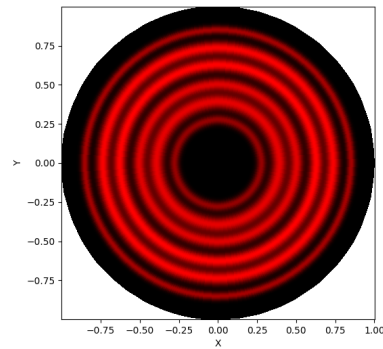
Table 4: Fit parameters for D_2 -Line

To complete this section we wanted to show a reconstruction of the image we saw on the live view. Therefore we used our fitted function for each line as the radial part of a plot in polar coordinates which is rotational invariant with respect to φ . The brightness is proportional to the intensity.

It is important to mention that this is **not** exactly what we saw on the screen. Due to the summarization by the software over all intensities along a shell from r to $r + \Delta r$ the angular dependence gets lost in our data so it is not reversible. Nevertheless this is not a big deal due to the fact that the theoretical result would be perfectly symmetric anyway so this is just a demonstration on what to expect instead of a exact measurement. So it is important to keep that in mind when looking at the graphics in [Figure 3.3](#)



(a) Image of the D_1 -lines at $I = 12$ A



(b) Image of the D_2 -lines at $I = 12$ A

Figure 3.3: Reconstruction of the image from FPI by plotting our fitted function as the radial part in polar coordinates.

3.3 Landé-factors

Now that we collected all necessary data we can begin with analyzing them. We already saw in Equation 5 that the Zeeman-energy can be calculated by $E_{Zee} = m_j g_j \mu_B B$ which can be expressed in terms of frequencies too:

$$m_j g_j = \frac{E_{Zee}}{\mu_B B} = \frac{h \nu_{Zee}}{\mu_B B} \quad (14)$$

This allows us to calculate the Landé-factors g_j by using the following relations for the D_1 -line:

$$\begin{aligned} \Delta \nu_{\pi_1} &= \left(\frac{1}{2} g(S_{1/2}) + \frac{1}{2} g(P_{1/2}) \right) \frac{\mu_B B}{h} \\ \Delta \nu_{\pi_2} &= \left(-\frac{1}{2} g(S_{1/2}) - \frac{1}{2} g(P_{1/2}) \right) \frac{\mu_B B}{h} \\ \Delta \nu_{\sigma_1^-} &= \left(\frac{1}{2} g(S_{1/2}) - \frac{1}{2} g(P_{1/2}) \right) \frac{\mu_B B}{h} \\ \Delta \nu_{\sigma_2^+} &= \left(-\frac{1}{2} g(S_{1/2}) + \frac{1}{2} g(P_{1/2}) \right) \frac{\mu_B B}{h} \end{aligned}$$

Note that $\Delta \nu_i$ is the frequency shift from the expected transition-frequency without a magnetic field. The relations for the second line are very similar but they won't be listed here. Since we cannot measure any absolute frequencies we need to combine the equations above to get several expressions for the Landé g-factors in dependence of a frequency difference $\Delta \nu_{i,j}$ between transitions i and j :

$$\begin{aligned} g(S_{1/2}) &= \frac{h}{2\mu_B B} (\Delta \nu_{\sigma_2^+, \sigma_1^-} + \Delta \nu_{\pi_2, \pi_1}) \\ g(P_{1/2}) &= \frac{h}{2\mu_B B} (\Delta \nu_{\sigma_2^+, \sigma_1^-} - \Delta \nu_{\pi_2, \pi_1}) \end{aligned}$$

The frequency differences $\Delta \nu_{i,j}$ can easily be obtained from Table 3 while B can be calculated from Equation 9. We calculated both Landé-factors present in the D_1 -transition for every magnetic field we measured and took the average as our result:

I	9 A	10 A	11 A	12 A	Mean
$g(S_{1/2})$	2,302	2,302	2,378	2,284	2,316
$g(P_{1/2})$	0,770	0,752	0,824	0,760	0,776

Table 5: Landé-factors from D_1 -data

Analogous the Landé-factors for the D_2 -transitions can be obtained from the following formulas:

$$\begin{aligned} g(S_{1/2}) &= \frac{h}{2\mu_B B} (\Delta \nu_{\sigma_2^+, \sigma_1^-} + \Delta \nu_{\pi_2, \pi_1}) \\ g(S_{1/2}) &= \frac{h}{4\mu_B B} (3\Delta \nu_{\sigma_2^+, \sigma_1^-} - \Delta \nu_{\sigma_1^+, \sigma_2^-}) \\ g(S_{1/2}) &= \frac{h}{4\mu_B B} (3\Delta \nu_{\pi_2, \pi_1} + \Delta \nu_{\sigma_1^+, \sigma_2^-}) \\ g(P_{3/2}) &= \frac{h}{2\mu_B B} (\Delta \nu_{\sigma_2^+, \sigma_1^-} - \Delta \nu_{\pi_2, \pi_1}) \\ g(P_{3/2}) &= \frac{h}{4\mu_B B} (\Delta \nu_{\sigma_2^+, \sigma_1^-} + \Delta \nu_{\sigma_1^+, \sigma_2^-}) \\ g(P_{3/2}) &= \frac{h}{2\mu_B B} (\Delta \nu_{\pi_2, \pi_1} + \Delta \nu_{\sigma_1^+, \sigma_2^-}) \end{aligned}$$

One can see that we got various equations for each $g(S_{1/2})$ and $g(P_{3/2})$, which is useful so that we can calculate all of them for all magnetic fields. This leaves us with enough data to take the average and get a hopefully accurate result. In Table 6 is our data for each magnetic field but averaged over the different formulas.

I	9 A	10 A	11 A	12 A	Mean
$g(S_{1/2})$	2,271	2,267	2,326	2,319	2,296
$g(P_{3/2})$	1,114	1,242	1,393	1,516	1,316

Table 6: Landé-factors from D_2 -data averaged over the different formulas

This leaves us with the final Landé g-factors seen in Table 7. For our experimental setup they are quite accurate and sufficient for estimating different behaviors. Although for scientific research the error is too big and a more complex setup would be needed.

Landé-factor	Our value	theoretical value	error
$g(S_{1/2})$	2,301	2	15,1%
$g(P_{1/2})$	0,776	2/3	16,4%
$g(P_{3/2})$	1,316	4/3	1,3%

Table 7: Final Landé-factors

What is worth mentioning is that the averaging over multiple different formulas for $g(P_{3/2})$ in fact led to a more accurate result and a smaller error.

3.4 Clebsch-Gordan coefficients

We've seen in section 1 that one can describe the emission of light out of a certain system, e.g. an atom in the state $P_{3/2}$ as an emitting source, by using a coupled system. Now the CGK come in handy, to determine all possible dipole transitions, where each squared coefficient equals the probability of transition for the specific state. These values can be calculated analytically and now we want to determine them by our data. First of all the CGK for the σ_2^- and σ_1^+ transition are assured to be one, as we are only interested in dipole transitions, i.e. $\Delta m = 0, \pm 1$. Now to determine the remaining four coefficients, we'll take a look at the ratio of both possible transitions (Figure 1.1) for $P_{3/2}(m_j = +\frac{1}{2})$ as well as for $P_{3/2}(m_j = -\frac{1}{2})$. When starting in one of them, only two decays are possible, as depicted in the previously mentioned figure. Therefore it is sensible that one would calculate the ratio, so that we know in which proportions the σ_1^-/σ_2^+ transition will appear in respect to the π_2/π_1 transition. In order to calculate the mentioned ratios, we'll use the amplitudes of the Gauß fit displayed in Table 4. As the intensity of measured rays is correlated to the number of photons detected, which is in turn also correlated to the likelihood of appearing, we are allowed to use the intensities to make a statement about transition probability. As we're speaking of likelihood, one has to make the constraint, that one transition **needs** to appear, so to speak, the probabilities have to add up to one for each of the four excited states. First we calculate the needed ratios for which one will get the following:

$$\frac{I(\sigma_1^-)}{I(\pi_2)} = \frac{2,206 \cdot 10^{-4}}{3,795 \cdot 10^{-4}} \approx 0,5813$$

$$\frac{I(\sigma_2^+)}{I(\pi_1)} = \frac{2,462 \cdot 10^{-4}}{3,302 \cdot 10^{-4}} \approx 0,7456$$

Now that the ratios are known, we can use the constraint pointed out earlier to finally determine our normalized transition probabilities, which are noted below:

But we're not finished, because the transition probability equals the squared CGK, so in order to get our final values we need to take the square root. Doing this leads to the coefficients shown in Table 9.

As one can see, the calculated CGK are quit precise with a tolerable average error of exactly 7%. This means that our measurement method and setup was good, although the apparatuses were very sensitive, thinking of

transition	σ_2^-	π_2	σ_2^+	σ_1^-	π_1	σ_1^+
probability	1	0.6324	0.4271	0.3676	0.5729	1

Table 8: Transition probability

CGK	Our value	theoretical value	error
σ_1^-	0,6063	0,5774	5,01%
σ_1^+	1	1	0%
σ_2^-	1	1	0%
σ_2^+	0,6535	0,5774	13,18%
π_1	0,7569	0,8165	7,20%
π_2	0,7952	0,8165	2,61%

Table 9: Calculated CGK

the FPI and Lyot filter. Maybe one would achieve better results by optimizing the alignment of the FPI, so that the $D2$ lines will appear sharper and will not effect each other due to their natural linewidth.

4 Conclusion and discussion of the results

The results of our experiment successfully demonstrate the splitting of the spectral lines from the sodium vapor lamp under influence of a magnetic field. This verifies our theoretical prediction as well as the behavior of the anomalous Zeeman effect.

Even the qualitative determination of the Landé g-factors led to acceptable results from which one could draw conclusions to the intra-atomic processes if they were not predicted theoretically yet. Furthermore we were able to show macroscopic phenomena of quantum physics which made calculating the Clebsch-Gordan coefficients possible.

To explain the deviations from the theoretical results there are some major error-sources.

One is the alignment of the FPI. This interferometer is very sensitive to the slightest touch which made aligning it demanding. Nevertheless it must be aligned as perfectly as possible due to a minor misalignment leading to an relatively bad image. So by taking even more time for this process one could enhance the resulting image and thus decrease the error.

Not only the human tolerances were responsible for the errors but instrumental limitations as well. We saw in [Figure 2.3](#) that the magnetic field was homogeneous to a certain degree but for high precision results the deviations within the important range in which the lamp sat were still too big. Thus a newer and better electromagnet would decrease the error further.

To conclude everything, the experiment provided a thorough exploration of the Zeeman effect and as well aligned with the quantum mechanical theory. Additionally it gave us the chance to further increase our knowledge and we were able to learn how to deal with different instruments in order to get meaningful results.

List of Figures

1.1	Energy term diagram of the two D-lines, figure from [5]	3
1.2	Intensity profile of dipole radiation for π -transition (a) and σ^\pm -transition (b) and (c). R and L describe right- and leftcircular polarization and S and P linear polarizations. Figure from [5]	5
1.3	construction of a Lyot filter, figure from [6]	6
1.4	ray path in a FPI, figure from [7]	6
2.1	Setup	7
2.2	Illustration on how the perspective changes the observed polarization for $\mathbf{B} \propto \hat{z}$	7
2.3	Magnetic induction in various positions of the \mathbf{B} -field to verify the homogeneity, values in mT for $I = 5 \text{ A}$	8
2.4	Magnetic induction from measured data	8
2.5	Schematic for the dimensions inside the FPI, not to scale	9
3.1	Plots necessary for determining the correction function	10
3.2	Measured spectrum of the D_1 - and D_2 -line in the magnetic field with a correspondign fit	10
3.3	Reconstruction of the image from FPI by plotting our fitted function as the radial part in polar coordinates.	11

List of Tables

1	CGK for D_1 -Line	4
2	CGK for D_2 -Line	4
3	Fit parameters for D_1 -Line	11
4	Fit parameters for D_2 -Line	11
5	Landé-factors from D_1 -data	12
6	Landé-factors from D_2 -data averaged over the different formulas	13
7	Final Landé-factors	13
8	Transition probability	14
9	Calculated CGK	14

References

- [1] Pieter Zeeman. Über einen einfluss der magnetisierung auf die natur des von einer substanz emittierten lichtes. <https://archive.org/details/verhandlungende24berlgoog/page/n254/mode/2up?view=theater>, 1896. [Accessed 02-11-2024].
- [2] The Nobel Prize in Physics 1902 — nobelprize.org. <https://www.nobelprize.org/prizes/physics/1902/summary/>. [Accessed 02-11-2024].
- [3] Harold J Metcalf and Peter Van der Straten. *Laser cooling and trapping*. Springer Science & Business Media, 1999.
- [4] Prof. Dr. Heiko Rieger. Theoretische physik iii. <https://www.rieger.uni-saarland.de/homepage/teaching/SS2024/TP3-Skript.pdf>, 2012. [Accessed 04-11-2024].
- [5] Saran Shaju. Zeeman-effekt. <https://www.uni-saarland.de/fileadmin/upload/fakultaet-nt/fopra/AnleitungenDeutsch/Zeeaman.pdf>, 2017. [Accessed 02-11-2024].
- [6] Wolfgang Demtröder. *Laserspektroskopie: Grundlagen und Techniken*. Springer-Verlag, 2007.
- [7] Chung-Ping Chang, Pi-Cheng Tung, Lih-Horng Shyu, yung-cheng Wang, and Eberhard Manske. Fabry-perot displacement interferometer for the measuring range up to 100 mm. *Measurement*, 46:4094–4099, 12 2013. doi: 10.1016/j.measurement.2013.06.029.
- [8] Wolfgang Demtröder. *Experimentalphysik*, volume 2. Springer, 2003.